The Astrophysical Journal, 851:117 (9pp), 2017 December 20 https://doi.org/10.3847/1538-4357/aa9ce4

Theory and Transport of Nearly Incompressible Magnetohydrodynamics Turbulence. III. Evolution of Power Anistropy in Magnetic Field Fluctuations throughout the Heliosphere

L. Adhikari[1], G. P. Zank[1,2], D. Telloni[3], P. Hunana[1,2], R. Bruno[4], and D. Shiota[5,6]
[1] Center for Space Plasma and Aeronomic Research (CSPAR), University of Alabama in Huntsville, Huntsville, AL 35899, USA
[2] Department of Space Science, University of Alabama in Huntsville, Huntsville, AL 35899, USA
[3] INAF—Astrophysical Observatory of Torino, Via Osservatorio 20, I-10025 Pino Torinese, Italy
[4] INAF-IAPS Instituto di Astrofisica e Planetologia Spaziali, Via del Fosso del Cavaliere 100, I-00133 Roma, Italy
[5] Institute for Space-Earth Environmental Research, Nagoya University, Nagoya, Aichi 464-8601, Japan
[6] National Institute of Information and Communications Technology (NICT), Koganei, Tokyo, 184-8795, Japan
Received 2017 October 2; revised 2017 November 14; accepted 2017 November 21; published 2017 December 19

Abstract

A theoretical model that describes the evolution of the power anisotropy in the energy-containing and inertial ranges throughout the heliosphere is developed for three possibilities: (i) no in situ sources of turbulence; (ii) stream-shear sources of 2D and slab turbulence; and (iii) a fully driven turbulence model that includes both stream-shear driving and a pickup ion source of slab turbulence. At the inner boundary (1 au), we assume that the ratios of the 2D to slab fluctuating magnetic energy variances in the energy-containing range are 80:20, 70:30, 60:40, and 55:45. For case (i), $\langle B_{2D}^2\rangle/\langle b_{slab}^2\rangle$ in the energy-containing range increases monotonically throughout the heliosphere, whereas the inertial range ratio increases until ∼20 au and then decreases. For case (ii), the energy-containing range ratio increases initially and then remains approximately constant and ordered beyond ∼2 au, according to the inner boundary assumptions. The inertial range ratio for the 80:20 case increases with heliocentric distance, whereas for the 70:30, 60:40, and 55:45 cases, the rations increase between ∼2 to ∼10–20 au, and then generally decrease at larger heliocentric distances. For case (iii), the energy-containing and inertial range ratios increase initially, remain approximately constant and increase slightly, respectively, and then decrease more rapidly between ∼8 and 30 au, and more gradually thereafter, approaching a ratio of ∼1 at 75 au. We present preliminary results that show the power anisotropy in magnetic field fluctuations observed by *Ulysses* spacecraft increasing with heliocentric distance from ∼1.5 to 4.5 au.

Key words: magnetohydrodynamics (MHD) – turbulence

1. Introduction

The nature of fluctuations in the solar wind is complicated and not yet fully understood. It is thought that solar wind fluctuations are highly anisotropic in the presence of a large-scale magnetic field $\boldsymbol{B}_0$ (Montgomery & Turner 1981; Matthaeus et al. 1990; Narita et al. 2010b) in that velocity and magnetic field fluctuations vary more rapidly in the direction perpendicular to $\boldsymbol{B}_0$ than parallel to $\boldsymbol{B}_0$. Anisotropy is a local property of turbulence that can modify solar wind turbulence and affects the propagation and acceleration of cosmic rays (Bieber et al. 1996; Zank et al. 1998; Shalchi et al. 2006), and the heating of interplanetary plasma (Velli 2003, for example). Dasso et al. (2005) suggested that solar wind fluctuations in the fast and slow solar wind exhibit different anisotropy properties. The anisotropy of solar wind fluctuations during solar minimum and maximum can also have different characteristics (Smith 2003). Several authors have studied anisotropy in the energy spectrum of MHD turbulence with respect to the magnetic field (Horbury et al. 2008; Podesta 2009; Narita et al. 2010a; Wicks et al. 2010; Bruno & Telloni 2015; Zank et al. 2017a).

Anisotropy in magnetic field fluctuations has also been studied by calculating the variance of magnetic field fluctuations. Robinson & Rusbridge (1971), Zweben et al. (1979), and Belcher & Davis (1971) calculated the variance of magnetic field fluctuations to study anisotropy in a laboratory plasma and the solar wind, respectively, in that they calculated the variances of magnetic field fluctuations in the direction parallel and perpendicular to the large-scale magnetic field. Anisotropy in solar wind fluctuations has also been studied using single-spacecraft data sets by calculating the power as a function of parallel and perpendicular wave vectors, respectively, relative to the mean magnetic field (Montgomery 1982; Matthaeus et al. 1990; Bieber et al. 1996; Milano et al. 2004; Dasso et al. 2005; Ruiz et al. 2011). Furthermore, Matthaeus et al. (2005), Dasso et al. (2008), Weygand et al. (2009), Osman & Horbury (2007) used multi-spacecraft data sets and calculated correlation functions in the direction parallel and perpendicular to the mean magnetic field to study anisotropy. Moreover, anisotropy has also been studied by well-documented theoretical and numerical methods (Montgomery & Turner 1981; Shebalin et al. 1983; Grappin 1986; Grappin et al. 1993; Goldreich & Sridhar 1995; Ghosh et al. 1998; Dong et al. 2014; Verdini & Grappin 2015, 2016). Furthermore, Verdini & Grappin (2016) also suggested that the evolution of the turbulent spectrum depends strongly on its initial anisotropy.

In this manuscript, our focus is the study of the evolution of turbulence anisotropy in the inertial range throughout the heliosphere using the nearly incompressible (Zank & Matthaeus 1991, 1992) turbulence transport model equations (Zank et al. 2017a; see also Adhikari et al. 2017a, 2017b). We also present a preliminary result that shows the evolution of the power anisotropy in magnetic field fluctuations observed by the *Ulysses* spacecraft from ∼1.5 to ∼4.5 au. Zank et al. (2017a) developed coupled 2D and slab turbulence transport model equations

appropriate to a $\beta \sim 1$ plasma (with β the thermal to magnetic pressure ratio) following the Hunana & Zank (2010) inhomogeneous nearly incompressible description of NI MHD turbulence. The Zank et al. (2017a) turbulence transport model equations describe the energy-containing range of solar wind turbulence. To study anisotropy in the inertial range, we derive a theoretical model using dimensional analysis to relate the power spectrum of magnetic field fluctuations in the energy-containing and inertial range. Slab and 2D turbulence can be distinguished by the orientation of the wave vector of the fluctuations relative to the mean magnetic field. In the former case, the wave vector is parallel to the mean magnetic field, whereas for 2D turbulence, the wave vectors of the fluctuations are perpendicular to the mean magnetic field.

Several studies have shown that the slow solar wind at 1 au contains a majority population of 2D fluctuations and a minority slab component (Zank & Matthaeus 1992; Bieber et al. 1996; Dasso et al. 2005). Fluctuations in fast wind appear to be more isotropic, while in slow wind they are more anisotropic. However, there are times when the slow wind shows exactly the same features as fast wind, the only difference being the lower bulk speed (D'Amicis & Bruno 2015). Theoretically and observationally, it is found that the ratio between 2D and slab turbulence energy is 80:20 (Zank & Matthaeus 1992; Bieber et al. 1996). This ratio can change depending on whether measurements are made in the fast or slow solar wind; at solar maximum or minimum; and at higher or lower latitudes. Zank et al. (2017a), Adhikari et al. (2017b) calculated the 2D and slab turbulent quantities from 1 to 75 au, assuming an inner boundary energy ratio at 1 au of 80:20 between 2D and slab turbulence. Later, Adhikari et al. (2017a) solved the 2D and slab turbulence transport model equations for different inner boundary energy ratios, 80:20, 70:30, 60:40, and 55:45, and found that the intensities of different turbulence quantities depended on the assumed inner boundary energy ratio, even though the quantities exhibit similar trends for the different ratios. Adhikari et al. (2017a) extended the Zank et al. (2017a) and Adhikari et al. (2017b) models by including a shear source of slab turbulence. The inclusion of a shear source of slab turbulence (Adhikari et al. 2017a) yielded slab quantities that are more reasonable in comparison to solutions that do not have a stream-shear source of slab turbulence (Adhikari et al. 2017a, 2017b; Zank et al. 2017a).

The outline of the manuscript is as follows. Section 2 presents a theoretical model relating the energy-containing to the inertial range. Section 3 presents the nearly incompressible turbulence transport model equations. Section 4 describes results of our theory, and Section 5 provides a discussion and conclusions.

2. Theory

In this section, we derive a theoretical model that describes the power anisotropy in magnetic field fluctuations as a function of the 2D and slab fluctuating magnetic energy and the corresponding correlation lengths. In constructing a transport model for turbulence in an inhomogeneous flow, there is an implicit assumption (Matthaeus et al. 1996; Zank et al. 1996a, 2012) that the inertial range of the turbulence spectrum is self-similar with the rate of energy input into the inertial range exactly balancing the dissipation rate. As is well-known in the case of MHD, this leads to the inertial range possessing a power-law spectrum of either the Kolmogorov or Iroshnikov–Kraichnan (I-K) forms. Zank et al. (2017a) derived an expression for the energy spectrum as a superposition of the majority 2D plus the minority slab component in the case of homogeneous $\beta \sim 1$ NI MHD (Zank et al. 2017b). The key point is that although the turbulence transport models represent a theory for the energy-containing fluctuations, the decay of these fluctuations is included by invoking a Kolmogorov/I-K phenomenology for the inertial range. The turbulence transport model therefore computes the rate at which energy enters (and dissipates from) the inertial range, for which we know the exact form. As the Zank et al. (2017a) theory for NI MHD describes the energy in both the 2D and slab components for a plasma beta $\sim$1 or $\ll$1, we can use these results to compute the power anisotropy in 2D and slab fluctuations in the inertial range as well.

We use dimensional analysis to relate the power spectrum of the magnetic field fluctuations in the energy-containing and inertial range. The correlation tensor $P_{ij}(\boldsymbol{k})$ for fluctuations can be expressed (e.g., Zank 2014) as

$$P_{ij}(\boldsymbol{k}) = A(k_{||}, k_{\perp})\left[\delta_{ij} - \frac{k_i k_j}{k^2}\right], \tag{1}$$

where k is a wave vector; $k_{||}$ and $k_{\perp}$ are parallel and perpendicular wave vectors in the direction parallel and perpendicular to the magnetic field; and δ_{ij} is the delta function. $A(k_{||}, k_{\perp})$ is a function of the wave vector that has to be formulated to complete the correlation tensor (Equation (1)). For this, we specify the geometry of the magnetic turbulence (i.e., 2D or slab), and the spectrum of the magnetic field fluctuations (i.e., k^{-1} for the energy-containing range or $k^{-5/3}$ for the inertial range).

For a 1D slab model, $\delta B^{\rm slab}(r) = \delta B^{\rm slab}(z)$, where δB is the turbulent/fluctuating magnetic field amplitude, r is a coordinate system, and z is the direction of the magnetic field, the function $A(k_{||}, k_{\perp})$ is expressed as (Zank 2014)

$$A^{\rm slab}(k_{||}, k_{\perp}) = g^{\rm slab}(k_{||})\frac{\delta(k_{\perp})}{k_{\perp}}, \tag{2}$$

where $g^{\rm slab}(k_{||})$ is a function of the parallel wave vector, and $\delta(k_{\perp})$ is the delta function of the perpendicular wave vector. Similarly, for 2D turbulence $\delta B^{\rm 2D}(r) = \delta B^{\rm 2D}(x, y)$, the function $A(k_{||}, k_{\perp})$ is (Zank 2014)

$$A^{\rm 2D}(k_{||}, k_{\perp}) = g^{\rm 2D}(k_{\perp})\frac{\delta(k_{||})}{k_{\perp}}, \tag{3}$$

where $g^{\rm 2D}(k_{\perp})$ is a function of the perpendicular wave vector, and $\delta(k_{||})$ is the delta function of the parallel wave vector. We prescribe the functions g^{2D} and g^{slab} as $g = Ck^{-1}$ and $g = Dk^{-5/3}$ for the energy-containing and inertial range, respectively. The parameters C and D are constants. From Equations (1) and (2) we obtain

$$\begin{aligned} P_{ij}^{\rm slab}(\boldsymbol{k}) &= g^{\rm slab}(k_{||})\frac{\delta(k_{\perp})}{k_{\perp}}\left[\delta_{ij} - \frac{k_i k_j}{k^2}\right], \\ &= g^{\rm slab}(k_{||})\frac{\delta(k_{\perp})}{k_{\perp}}\delta_{ij} \text{ if } i, j = x, y, \end{aligned} \tag{4}$$

and $P_{iz} = 0 = P_{zj}$ (Zank 2014) for slab turbulence. The variance of the magnetic field fluctuations for slab turbulence

in the energy-containing range is then (Zank 2014)

$$\langle b^2_{\rm slab}\rangle_{\rm ER} = 2\int\int\int g^{\rm slab}(k_{||})\frac{\delta(k_\perp)}{k_\perp}k_\perp d\theta dk_\perp dk_{||},$$
$$= 4\pi\int g^{\rm slab}(k_{||})dk_{||}, \quad (5)$$

with $g^{\rm slab}(k_{||}) = C^{\rm slab}k_{||}^{-1}$. Integrating Equation (5) from k_{inj} to $(l_b^{\rm slab})^{-1}$ gives

$$C^{\rm slab}_{\rm ER} \equiv \frac{\langle b^2_{\rm slab}\rangle_{\rm ER}}{\log\left(\frac{(l_b^{\rm slab})^{-1}}{k_{inj}}\right)}. \quad (6)$$

In Equation (6), k_{inj} is a large-scale injection wave number and $l_b^{\rm slab}$ is the correlation length of the variance of the slab magnetic field fluctuations. ER denotes the energy-containing range.

Similarly, from Equations (1) and (3) we obtain the correlation tensor for 2D turbulence (Zank 2014) as

$$P^{\rm 2D}_{ij}(\boldsymbol{k}) = \begin{cases} g^{\rm 2D}(k_\perp)\frac{\delta(k_{||})}{k_\perp}\left[\delta_{ij} - \frac{k_ik_j}{k^2}\right], & \text{if } i,j = x,y, \\ 0, & \text{if } i \text{ or } j = z, \end{cases} \quad (7)$$

and the variance of the magnetic field fluctuations as

$$\langle B^2_{\rm 2D}\rangle_{\rm ER} = \int\int\int g^{\rm 2D}(k_{||})\frac{\delta(k_{||})}{k_\perp}\left(\delta_{ij} - \frac{k_ik_j}{k^2}\right)k_\perp d\theta dk_\perp dk_{||},$$
$$= 2\pi\int g^{\rm 2D}(k_\perp)dk_\perp J_0(k_\perp r), \quad (8)$$

where $J_0(k_\perp r)$ is a Bessel function of zeroth order. We use the limit $k_\perp r \to 0$, which gives $J_0(k_\perp r) \to 1$ (Zank 2014). Again, with $g^{\rm 2D}(k_\perp) = C^{\rm 2D}_{\rm ER}k_\perp^{-1}$, and integrating Equation (8) from k_{inj} to $(l_b^{\rm 2D})^{-1}$ gives

$$C^{\rm 2D}_{\rm ER} \equiv \frac{\langle B^2_{\rm 2D}\rangle_{\rm ER}}{\log\left(\frac{(l_b^{\rm 2D})^{-1}}{k_{inj}}\right)}, \quad (9)$$

where $l_b^{\rm 2D}$ is the correlation length of the 2D magnetic field fluctuations. On dividing Equation (6) by Equation (9), we obtain

$$\frac{C^{\rm 2D}_{\rm ER}}{C^{\rm slab}_{\rm ER}} = \frac{\langle B^2_{\rm 2D}\rangle_{\rm ER}}{\langle b^2_{\rm slab}\rangle_{\rm ER}}\frac{\log\left(\frac{(l_b^{\rm slab})^{-1}}{k_{inj}}\right)}{\log\left(\frac{(l_b^{\rm 2D})^{-1}}{k_{inj}}\right)}. \quad (10)$$

In the limit $k_{inj} \to 0$, (10) reduces to

$$\frac{C^{\rm 2D}_{\rm ER}}{C^{\rm slab}_{\rm ER}} \sim \frac{\langle B^2_{\rm 2D}\rangle_{\rm ER}}{\langle b^2_{\rm slab}\rangle_{\rm ER}}. \quad (11)$$

Equation (10) describes the ratio of the 2D and slab magnetic energy densities associated with the energy-containing range. On using this result, we derive the ratio of the 2D and slab variances of the magnetic field fluctuations in the inertial range. Let k_b be the wave number that separates the energy-containing range and the inertial range so that $Ck^{-1}|_{k_b} = Dk^{-5/3}|_{k_b}$, which yields $D = Ck_b^{2/3}$. Thus, the power spectrum in the inertial range can be written as $Ck_b^{2/3}k^{-5/3}$. Hence, $C^{\rm 2D}(k_b^{\rm 2D})^{2/3}k_\perp^{-5/3}$ and $C^{\rm slab}(k_b^{\rm slab})^{2/3}k_{||}^{-5/3}$ are the spectra in the inertial range for 2D and slab turbulence, respectively.

The variance of the slab magnetic field fluctuations in the inertial range can be written as

$$\langle b^2_{\rm slab}\rangle_{\rm IR} = 2\int\int\int g^{\rm slab}(k_{||})\frac{\delta(k_\perp)}{k_\perp}k_\perp d\theta dk_{||}dk_\perp,$$
$$= 4\pi\int g^{\rm slab}(k_{||})dk_{||}.$$

Suppose we consider the anisotropy in a wave number range $[k_1^{\rm slab}, k_2^{\rm slab}]$, where $k_1^{\rm slab}$ and $k_2^{\rm slab}$ are arbitrary wave numbers such that $k_b^{\rm slab} < k_1^{\rm slab} < k_2^{\rm slab}$. We then obtain by integrating the above equation from $k_1^{\rm slab}$ to $k_2^{\rm slab}$,

$$\langle b^2_{\rm slab}\rangle_{\rm IR} \equiv C^{\rm slab}_{\rm ER}(k_b^{\rm slab})^{2/3}\int_{k_1^{\rm slab}}^{k_2^{\rm slab}} k_{||}^{-5/3}dk_{||},$$
$$= \frac{3}{2}C^{\rm slab}_{\rm ER}(k_b^{\rm slab})^{2/3}((k_1^{\rm slab})^{-2/3} - (k_2^{\rm slab})^{-2/3}). \quad (12)$$

Here, $g^{\rm slab}(k_{||}) = C^{\rm slab}_{\rm ER}(k_b^{\rm slab})^{2/3}k_{||}^{-5/3}$ is used. IR denotes the inertial range. Similarly, the variance of the 2D magnetic field fluctuations in the inertial range is

$$\langle B^2_{\rm 2D}\rangle_{\rm IR} = \int\int\int g^{\rm 2D}(k_{||})\frac{\delta(k_\perp)}{k_\perp}\left(\delta_{ij} - \frac{k_ik_j}{k^2}\right)k_\perp d\theta dk_\perp dk_{||},$$
$$= 2\pi\int g^{\rm 2D}(k_\perp)dk_\perp.$$

Integrating the above equation from $k_1^{\rm 2D}$ to $k_2^{\rm 2D}$, where $k_b^{\rm 2D} < k_1^{\rm 2D} < k_2^{\rm 2D}$, we obtain

$$\langle B^2_{\rm 2D}\rangle_{\rm IR} \equiv C^{\rm 2D}_{\rm ER}(k_b^{\rm 2D})^{2/3}\int_{k_1^{\rm 2D}}^{k_2^{\rm 2D}} k_\perp^{-5/3}dk_\perp,$$
$$= \frac{3}{2}C^{\rm 2D}_{\rm ER}(k_b^{\rm 2D})^{2/3}((k_1^{\rm 2D})^{-2/3} - (k_2^{\rm 2D})^{-2/3}). \quad (13)$$

Here, $g^{\rm 2D}(k_\perp) = C^{\rm 2D}(k_b^{\rm 2D})^{2/3}k_\perp^{-5/3}$ is used. Dividing Equation (13) by Equation (12) gives the ratio of the variances of the 2D and slab magnetic field fluctuations in a section of the inertial range as

$$\frac{\langle B^2_{\rm 2D}\rangle_{\rm IR}}{\langle b^2_{\rm slab}\rangle_{\rm IR}} = \frac{C^{\rm 2D}_{\rm ER}}{C^{\rm slab}_{\rm ER}}\left(\frac{k_b^{\rm 2D}}{k_b^{\rm slab}}\right)^{2/3}\frac{((k_1^{\rm 2D})^{-2/3} - (k_2^{\rm 2D})^{-2/3})}{((k_1^{\rm slab})^{-2/3} - (k_2^{\rm slab})^{-2/3})},$$

which for $k_1^{\rm 2D} = k_1^{\rm slab}$ and $k_2^{\rm 2D} = k_2^{\rm slab}$ becomes

$$\frac{\langle B^2_{\rm 2D}\rangle_{\rm IR}}{\langle b^2_{\rm slab}\rangle_{\rm IR}} = \frac{C^{\rm 2D}_{\rm ER}}{C^{\rm slab}_{\rm ER}}\left(\frac{k_b^{\rm 2D}}{k_b^{\rm slab}}\right)^{2/3}. \quad (14)$$

Equations (10) and (14) yield the ratio of the variances of the 2D and slab magnetic field fluctuations in the inertial range,

$$\frac{\langle B^2_{\rm 2D}\rangle_{\rm IR}}{\langle b^2_{\rm slab}\rangle_{\rm IR}} = \frac{\langle B^2_{\rm 2D}\rangle_{\rm ER}}{\langle b^2_{\rm slab}\rangle_{\rm ER}}\left(\frac{l_b^{\rm slab}}{l_b^{\rm 2D}}\right)^{2/3}\frac{\log\left(\frac{(l_b^{\rm slab})^{-1}}{k_{inj}}\right)}{\log\left(\frac{(l_b^{\rm 2D})^{-1}}{k_{inj}}\right)}, \quad (15)$$

which in the limit $k_{inj} \to 0$ becomes

$$\frac{\langle B^2_{\rm 2D}\rangle_{\rm IR}}{\langle b^2_{\rm slab}\rangle_{\rm IR}} \sim \frac{\langle B^2_{\rm 2D}\rangle_{\rm ER}}{\langle b^2_{\rm slab}\rangle_{\rm ER}}\left(\frac{l_b^{\rm slab}}{l_b^{\rm 2D}}\right)^{2/3}. \quad (16)$$

We use Equation (15) to study the anisotropy of magnetic field fluctuations in the inertial range. In Equation (15), the turbulence parameters $\langle B_{2D}^2\rangle_{ER}$, $\langle b_{slab}^2\rangle_{ER}$, l_b^{slab}, and l_b^{2D} on the right-hand side are associated with the energy-containing range (Adhikari et al. 2017a, 2017b; Zank et al. 2017a). We use $k_{inj} \sim 1.07 \times 10^{-9}\,\mathrm{km}^{-1}$ in Equation (15), which corresponds to one solar rotation (~27 days). Equation (16) provides an asymptotic estimate of Equation (15).

3. Turbulence Model Equations

We solve the Zank et al. (2017a) coupled turbulence transport model equations to obtain the values of the turbulence parameters $\langle B_{2D}^2\rangle_{ER}$, $\langle b_{slab}^2\rangle_{ER}$, l_b^{slab}, and l_b^{2D} (see also Adhikari et al. 2017a, 2017b). The 1D steady-state 2D turbulence transport model equations in a spherical coordinate system r are

$$\begin{aligned}
&U\frac{d}{dr}\langle z^{\infty\pm 2}\rangle + \frac{U}{r}\langle z^{\infty\pm 2}\rangle + \frac{U}{r}E_D^{\infty}\\
&+ \frac{1}{r}\langle z^{\infty\pm 2}\rangle^{1/2}(\langle z^{\infty\pm 2}\rangle - E_D^{\infty})\\
&= -2\frac{\langle z^{\infty\pm 2}\rangle^2\langle z^{\infty\mp 2}\rangle^{1/2}}{L_{\infty}^{\pm}} + 2\frac{\langle z^{*\pm 2}\rangle^2\langle z^{*\mp 2}\rangle^{1/2}}{L^{*\pm}}\\
&+ 2C_{sh}^{\pm}\frac{r_0|\Delta U|V_{A0}^2}{r^2};
\end{aligned} \tag{17}$$

$$\begin{aligned}
&U\frac{dE_D^{\infty}}{dr} + \frac{U}{r}E_D^{\infty} + \frac{U}{r}E_T^{\infty}\\
&+ \frac{1}{2r}(E_D^{\infty} - \langle z^{\infty+2}\rangle^{1/2}\langle z^{\infty-2}\rangle^{1/2})(\langle z^{\infty+2}\rangle^{1/2} + \langle z^{\infty-2}\rangle^{1/2})\\
&= -E_D^{\infty}\left(\frac{\langle z^{\infty+2}\rangle\langle z^{\infty-2}\rangle^{1/2}}{L_{\infty}^{+}} + \frac{\langle z^{\infty-2}\rangle\langle z^{\infty+2}\rangle^{1/2}}{L_{\infty}^{-}}\right)\\
&+ E_D^{*}\left(\frac{\langle z^{*+2}\rangle\langle z^{*-2}\rangle^{1/2}}{L_{*}^{+}} + \frac{\langle z^{*-2}\rangle\langle z^{*+2}\rangle^{1/2}}{L_{*}^{-}}\right)\\
&+ 2C_{sh}^{E_D}\frac{r_0|\Delta U|V_{A0}^2}{r^2};
\end{aligned} \tag{18}$$

$$U\frac{dL_{\infty}^{\pm}}{dr} + \frac{U}{r}L_{\infty}^{\pm} + \frac{U}{2r}L_D^{\infty} - \frac{1}{2r}\langle z^{\infty\pm 2}\rangle^{1/2}(L_D^{\infty} - 2L_{\infty}^{\pm}) = 0; \tag{19}$$

$$\begin{aligned}
&U\frac{dL_D^{\infty}}{dr} + \frac{U}{r}L_D^{\infty} + \frac{U}{r}(L_{\infty}^{+} + L_{\infty}^{-})\\
&+ \frac{1}{2r}(L_D^{\infty}(\langle z^{\infty+2}\rangle^{1/2} + \langle z^{\infty-2}\rangle^{1/2})\\
&- 2L_{\infty}^{+}\langle z^{\infty-2}\rangle^{1/2} - 2L_{\infty}^{-}\langle z^{\infty+2}\rangle^{1/2}) = 0,
\end{aligned} \tag{20}$$

where $\langle z^{\infty\pm 2}\rangle$ is the energy in forward/backward propagating modes, E_D^{∞} is the residual energy, $L_{\infty}^{\pm}$ are correlation functions corresponding to $\langle z^{\infty\pm 2}\rangle$, and L_D^{∞} the correlation function for E_D^{∞}. The parameters $C_{sh}^{\pm}$ and $C_{sh}^{E_D}$ are parametrized strengths of the shear source of energy in forward (+) and backward modes (−) and the residual energy (E_D), respectively. Here, r_0(=1 au) is a reference location, ΔU is the difference between fast and slow solar wind speed, and V_{A0} is the Alfvén velocity at 1 au.

Similarly, the 1D steady-state slab turbulence transport model equations are

$$\begin{aligned}
&\left(U \mp V_{A0}\frac{r_0}{r}\right)\frac{d\langle z^{*\pm 2}\rangle}{dr} - (2b-1)\frac{U}{r}\langle z^{*\pm 2}\rangle\\
&+ 2\left(3b - \frac{1}{2}\right)\frac{U}{r}E_D^{*} \pm (4b-1)\frac{V_{A0}}{r_0}\left(\frac{r_0}{r}\right)^2 E_D^{*}\\
&\pm \frac{V_{A0}}{r_0}\left(\frac{r_0}{r}\right)^2\langle z^{*\pm 2}\rangle + \frac{1}{r}(\langle z^{*\pm 2}\rangle - E_D^{*})\langle z^{\infty\pm 2}\rangle^{1/2}\\
&= -2\frac{\langle z^{*\pm 2}\rangle\langle z^{\infty\pm 2}\rangle\langle z^{\infty\mp 2}\rangle^{1/2}}{L_{\infty}^{\pm}}\\
&- 2\frac{\langle z^{*\pm 2}\rangle^2\langle z^{*\mp 2}\rangle^{1/2}}{L_{*}^{\pm}} + 2C^{*\pm}_{sh}\frac{r_0|\Delta U|V_{A0}^2}{r^2} + \frac{f_D n_H^{\infty} U V_{A0}}{n_{sw}^0\tau_{ion}^0}\\
&\times \exp\left(\frac{-L}{r}\right);
\end{aligned} \tag{21}$$

$$\begin{aligned}
&U\frac{dE_D^{*}}{dr} - (2b-1)\frac{U}{r}E_D^{*} + 2\left(3b-\frac{1}{2}\right)\frac{U}{r}E_T^{*}\\
&- (4b-1)E_C^{*}\frac{V_{A0}}{r_0}\left(\frac{r_0}{r}\right)^2\\
&+ \frac{1}{2r}[E_D^{*}(\langle z^{\infty+2}\rangle^{1/2} + \langle z^{\infty-2}\rangle^{1/2}) - \langle z^{*-2}\rangle\langle z^{\infty+2}\rangle^{1/2}\\
&- \langle z^{*+2}\rangle\langle z^{\infty-2}\rangle^{1/2}]\\
&= -E_D^{*}\left(\frac{\langle z^{\infty+2}\rangle\langle z^{\infty-2}\rangle^{1/2}}{L_{\infty}^{+}} + \frac{\langle z^{\infty-2}\rangle\langle z^{\infty+2}\rangle^{1/2}}{L_{\infty}^{-}}\right)\\
&- E_D^{*}\left(\frac{\langle z^{*+2}\rangle\langle z^{*-2}\rangle^{1/2}}{L_{*}^{+}}\right.\\
&\left.+ \frac{\langle z^{*-2}\rangle\langle z^{*+2}\rangle^{1/2}}{L_{*}^{-}}\right) + 2C^{*E_D}_{sh}\frac{r_0|\Delta U|V_{A0}^2}{r^2};
\end{aligned} \tag{22}$$

$$\begin{aligned}
&\left(U \mp V_{A0}\frac{r_0}{r}\right)\frac{dL_{*}^{\pm}}{dr} - (2b-1)\frac{U}{r}L_{*}^{\pm} + 2\left(\frac{3}{2}b - \frac{1}{4}\right)\frac{U}{r}L_D^{*}\\
&\pm \left(2b - \frac{1}{2}\right)\frac{V_{A0}}{r_0}\left(\frac{r_0}{r}\right)^2 L_D^{*}\\
&\pm \frac{V_{A0}}{r_0}\left(\frac{r_0}{r}\right)^2 L_{*}^{\pm} + \frac{1}{r}\left(L_{*}^{\pm} - \frac{L_D^{*}}{2}\right)\langle z^{\infty\pm 2}\rangle^{1/2} = 0;
\end{aligned} \tag{23}$$

$$\begin{aligned}
&U\frac{dL_D^{*}}{dr} - 2\left(b-\frac{1}{2}\right)\frac{U}{r}L_D^{*} + 2\left(3b-\frac{1}{2}\right)\frac{U}{r}(L_{*}^{+} + L_{*}^{-})\\
&-(4b-1)(L_{*}^{+} - L_{*}^{-})\frac{V_{A0}}{r_0}\left(\frac{r_0}{r}\right)^2\\
&-\frac{1}{r}\left[\left(L_{*}^{-} - \frac{L_D^{*}}{2}\right)\langle z^{\infty+2}\rangle^{1/2}\right.\\
&\left.+\left(L_{*}^{+} - \frac{L_D^{*}}{2}\right)\langle z^{\infty-2}\rangle^{1/2}\right] = 0,
\end{aligned} \tag{24}$$

where $\langle z^{*\pm 2}\rangle$ is the slab energy in forward/backward propagating modes, E_D^{*} is the slab residual energy, $L_{*}^{\pm}$ are the correlation functions corresponding to $\langle z^{*\pm 2}\rangle$, and L_D^{*} the

Table 1
Boundary Values for the Cases of the 80:20, 70:30, 60:40, and 55:45 Energy Ratios between 2D and Slab Turbulence at 1 au (Adhikari et al. 2017a)

Parameters	80:20	70:30	60:40	55:45
$\langle z^{\infty +2}\rangle$ (km^2 s^{-2})	1600	1400	1200	1100
$\langle z^{\infty -2}\rangle$ (km^2 s^{-2})	160	140	120	110
E_D^{∞} (km^2 s^{-2})	−80	−70	−60	−55
L_{∞}^{+} (km^3 s^{-2})	2.95×10^9	2.58×10^9	2.21×10^9	2.03×10^9
L_{∞}^{-} (km^3 s^{-2})	2.65×10^8	2.32×10^8	1.99×10^8	1.82×10^8
L_D^{∞} (km^3 s^{-2})	-1.7×10^8	-1.49×10^8	-1.27×10^8	-1.16×10^8
$\langle z^{*+2}\rangle$ (km^2 s^{-2})	400	600	800	900
$\langle z^{*-2}\rangle$(km^2 s^{-2})	40	60	80	90
E_D^{*}(km^2 s^{-2})	−20	−30	−40	−45
L_{*}^{+} (km^3 s^{-2})	2.96×10^8	4.44×10^8	5.93×10^8	6.67×10^8
L_{*}^{-} (km^3 s^{-2})	1.66×10^8	2.49×10^8	3.33×10^8	3.75×10^8
L_D^{*} (km^3 s^{-2})	-4.25×10^7	-6.38×10^7	-8.5×10^7	-9.57×10^7

correlation function for E_D^*. The parameters $C^{*\pm}_{sh}$ and $C^{*\,E_D}_{sh}$ are the strengths of the stream-shear source of slab turbulence. The parameter L is the ionization cavity length scale, and f_D is the fraction of pickup ion (PUI) energy transferred into excited waves (Isenberg 2005). The parameter n_H^{∞} is the number density of interstellar neutrals entering the heliosphere, $\tau^0_{\rm ion}$ is the neutral ionization time at 1 au, n^0_{sw} is the solar wind density at 1 au, and $0 < b < 1$ is a constant.

The 2D and slab variances of magnetic field fluctuations and the corresponding correlation lengths are given by

$$\left\langle \frac{B^{\infty,*2}}{\mu_0 \rho} \right\rangle = \frac{\langle z^{\infty,*+2}\rangle + \langle z^{\infty,*-2}\rangle - 2E_D^{\infty,*}}{4}, \text{ and}$$

$$l_b^{\infty,*} = \frac{L_+^{\infty,*} + L_-^{\infty,*} - L_D^{\infty,*}}{\langle z^{\infty,*+2}\rangle + \langle z^{\infty,*-2}\rangle - 2E_D^{\infty,*}}, \quad (25)$$

where μ_0 is the magnetic permeability of free space and ρ is the solar wind density. In the above turbulence transport equations, "∞" indicates 2D turbulence, and "*" indicates slab turbulence.

The turbulence transport Equations (17)–(24) are appropriate to a $\beta \sim 1$ or $\ll 1$ plasma. However, with the creation of PUIs in the outer heliosphere, a naive estimate of the plasma beta that includes the contribution of hot PUIs yields $\beta \sim 4$ (e.g., Zank et al. 1996b; Zank 1999). However, as discussed by Zank et al. (2014) and Isenberg (1986), PUIs are not equilibrated with the background, higher-density solar wind (PUIs are less than 20% of the solar wind number density in the vicinity of the heliospheric termination shock located at ∼85–90 au), despite co-moving with the background flow. Consequently, the Alfvén speed, for example, is determined primarily by the background solar wind and the 2D turbulence is similarly determined by the background solar wind magnetic field and plasma. Incompressible turbulence (2D and slab) in the distant solar wind, even in the presence of PUIs, is therefore determined primarily by the incompressible background solar wind plasma and not by the PUIs. The solar wind plasma beta is $\ll 1$ (Zank et al. 1996b; Zank 1999; Adhikari et al. 2017b) when PUIs are excluded, making the NI MHD description in the $\beta \sim 1$, $\ll 1$ limit appropriate for the outer heliosphere. By contrast, we note that the large pressure contribution by PUIs not only modifies the propagation of compressible background solar wind plasma waves but also introduces distinct compressible PUI waves (Zank et al. 2014).

Table 2
Solar Wind Model Parameters Used in Solving Equations (17)–(24) (Adhikari et al. 2017b)

Parameters	Values	Parameters	Values
r_0	1 au	b	0.26
U	400 km s^{-1}	$\tau^0_{\rm ion}$	10^6 s
V_{A0}	40 km s^{-1}	$n^0_{\rm sw}$	5 cm^{-3}
ΔU	200 km s^{-1}	n_H^{∞}	0.1 cm^{-3}
L	8 au	α	0.2

4. Results

In this section, we calculate the evolution of power anisotropy in magnetic field fluctuations with increasing heliocentric distance from 1 to 75 au using Equation (15) for three cases: (i) no in situ sources of turbulence; (ii) stream-shear sources of 2D and slab turbulence only; and (iii) a PUI source of slab turbulence as well as the 2D and slab stream-shear sources. To calculate the evolution of power anisotropy for the three cases, we first solve the coupled turbulence transport Equations (17)–(24) for each case from 1 to 75 au. Then, we use Equation (25) to calculate the 2D and slab variances of the magnetic field fluctuations and the corresponding correlation lengths. These are used in Equation (15) to calculate the power anisotropy in the magnetic field fluctuations. In case (i), Equations (17)–(24) are solved without any sources of turbulence. In case (ii), Equations (17)–(24) are solved assuming stream-shear sources for the 2D and slab turbulence. Similarly, in case (iii), Equations (17)–(24) are solved assuming stream-shear sources of 2D and slab turbulence, and a PUI source of slab turbulence. We solve Equations (17)–(24) using a Runge–Kutta fourth-order method with the boundary conditions shown in Table 1. Table 1 shows the boundary values (1 au) of the turbulence parameters assuming initial energy ratios of 80:20, 70:30, 60:40, and 55:45 between 2D and slab turbulence. Here, we solve Equations (17)–(24) in each case for the boundary values corresponding to the 80:20, 70:30, 60:40, and 55:45 energy ratios. The solar wind parameters used in the numerical solutions are shown in Table 2. Similarly, the strengths of the stream-shear sources of 2D and slab turbulence and the PUI source of slab turbulence used for cases (i), (ii), and (iii) are shown in second, third, and fourth column of Table 3, respectively.

Table 3
Strengths of the Stream-shear Sources of 2D and Slab Turbulence, and the Pickup Ion Source of Slab Turbulence (Adhikari et al. 2017b)

Parameters	Case (i)	Case (ii)	Case (iii)
C_{sh}^{+}	0	0.9	0.9
C_{sh}^{-}	0	0.9	0.9
$C_{sh}^{E_D}$	0	−0.5	−0.5
C_{sh}^{*+}	0	0.3	0.3
C_{sh}^{*-}	0	0.3	0.3
$C^{*}{}_{sh}^{E_D}$	0	−0.17	−0.17
f_D	0	0	0.25

Figure 1 shows the evolution of power anisotropy as a function of heliocentric distance from 1 to 75 au in the absence of a source of turbulence. In Figure 1, the solid curves correspond to the power anisotropy in magnetic field fluctuations in the inertial range, and the dashed curves to those in the energy-containing range. The black, red, blue, and green curves correspond to the initial 80:20, 70:30, 60:40, and 55:45 energy ratios between 2D and slab turbulence in the energy-containing range. Figure 1 shows that the evolution of the $\langle B_{2D}^2\rangle/\langle b_{slab}^2\rangle$ ratio in the energy-containing range (dashed curves) for each initial energy ratio exhibits similar characteristics between 1 and 75 au. The evolution of the $\langle B_{2D}^2\rangle/\langle b_{slab}^2\rangle$ ratios in the inertial range for each energy ratio also behave similarly from 1–75 au. However, not surprisingly, the anisotropy increases with increasing ratio from 55:45 to 80:20 (green to black curves). Figure 1 shows that the ratio $\langle B_{2D}^2\rangle/\langle b_{slab}^2\rangle$ in the energy-containing range in the absence of a source of turbulence increases monotonically with increasing heliocentric distance, whereas the ratio $\langle B_{2D}^2\rangle/\langle b_{slab}^2\rangle$ in the inertial range increases until ∼20 au, and then decreases.

Figure 2 shows the evolution of the power anisotropy in magnetic field fluctuations as a function of heliocentric distance in the presence of stream-shear sources of 2D and slab turbulence. The ratio $\langle B_{2D}^2\rangle/\langle b_{slab}^2\rangle$ in the energy-containing range (dashed curves) exhibits similar trends for each of the initial energy ratios, as does $\langle B_{2D}^2\rangle/\langle b_{slab}^2\rangle$ in the inertial range (solid curves). $\langle B_{2D}^2\rangle/\langle b_{slab}^2\rangle$ in the energy-containing range increases initially, followed by a slight decrease, and then becomes approximately constant. Figure 2 shows that all the solid curves tend to a value close to ∼5 at 75 au, i.e., independent of the initial energy ratio at 1 au.

Figure 3 shows the evolution of the ratio of the 2D and slab magnetic field variances as a function of heliocentric distance in the presence of stream-shear sources of 2D and slab turbulence, and a PUI source of slab turbulence. The inclusion of the PUI source of slab turbulence, leads to a decrease in the ratio of the 2D and slab magnetic field variances in the energy-containing and inertial range beyond ∼5–6 au. The decrease is more rapid from ∼6 to ∼30 au and then more gradual until 75 au. The driving of turbulence by PUIs in the distant heliosphere drives the ratio $\langle B_{2D}^2\rangle/\langle b_{slab}^2\rangle$ for the inertial range to a value of approximately 1, which indicates that the fluctuations are almost isotropic.

Figure 4 shows the evolution of the power anisotropy in magnetic field fluctuations for different choices in the strength of the stream-shear sources of slab turbulence. Here, we fix the strengths of the stream-shear source of 2D turbulence as $C_{sh}^{\pm} = 0.9$ and $C_{sh}^{E_D} = -0.5$, and the strength of the PUI source of slab turbulence as $f_D = 0.25$. In Figure 4, we vary the

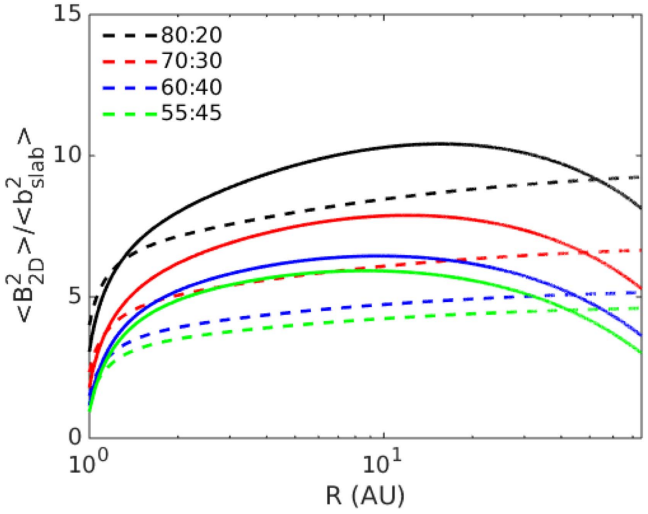

Figure 1. Evolution of the power anisotropy in magnetic field fluctuations as a function of heliocentric distance for different energy ratios between 2D and slab turbulence (case (i)). The solid curves correspond to the inertial range and the dashed curves to the energy-containing range.

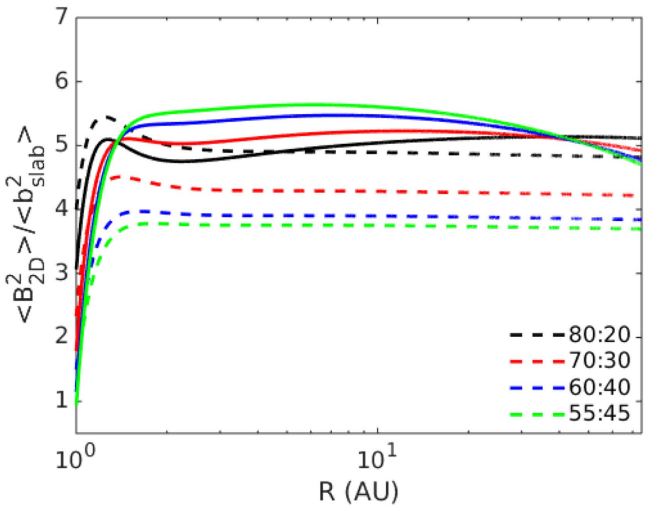

Figure 2. Evolution of the power anisotropy as a function of heliocentric distance for different 2D and slab energy ratios (case (ii)). The solid and dashed curves are as in Figure 1.

parameters for the stream-shear source of slab turbulence as $C^{*\pm}_{sh} = 0.45$ and $C^{*E_D}_{sh} = -0.25$ (top panel); $C^{*\pm}_{sh} = 0.6$ and $C^{*E_D}_{sh} = -0.33$ (middle panel); and $C^{*\pm}_{sh} = 0.9$ and $C^{*E_D}_{sh} = -0.5$ (bottom panel), i.e., the stream-shear source of slab turbulence increases. In Figure 4, the left column plots correspond to stream-shear sources of 2D and slab turbulence only, and the right column plots correspond to both stream-shear sources of 2D and slab turbulence and the PUI source of slab turbulence. Figure 4 shows that the ratio of the 2D and slab variances of magnetic field fluctuations in the inertial and energy-containing range decreases with increasing strength of stream-shear source of slab turbulence, showing that a stronger stream-shear source of slab turbulence reduces the anisotropy in magnetic field fluctuations. Furthermore, Figure 4 (left column) shows that the black curve (initial energy ratio 80:20) has a positive trend with heliocentric distance, while the blue, red, and green curves in the top and middle left panels show a radial decrease from ∼10–20 to 75 au. In the bottom-left plot of

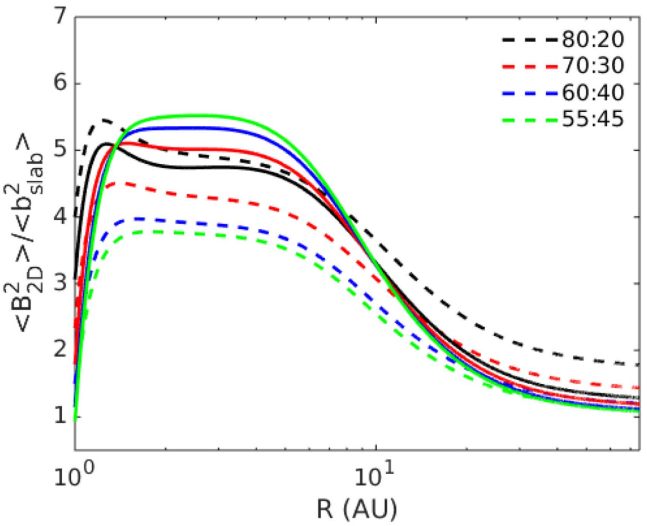

Figure 3. Evolution of the power anisotropy as a function of heliocentric distance for different energy ratios (case (iii)).

Figure 4, the solid black and red curves show a positive trend with heliocentric distance from ∼2 to 75 au. However, the blue and green curves increase with distance from ∼2 to ∼10 au, and then remain approximately constant until 75 au. In all cases, PUI driven turbulence yields essentially almost isotropic turbulence ($\langle B_{2D}^2\rangle/\langle b_{slab}^2\rangle \sim 1$). Of course, the eventual value of the ratio in the inertial range in the left column depends on the strength of the source term, but those values are essentially the same at 75 au regardless of the initial energy-containing ratio at 1 au i.e., the eventual ratio $\langle B_{2D}^2\rangle/\langle b_{slab}^2\rangle$ in the inertial range is essentially the same despite the initial disparity of the ratio in the energy-containing range.

5. Discussion and Conclusions

We studied the evolution of the power anisotropy in magnetic field fluctuations theoretically throughout the heliosphere for three cases: (i) no in situ sources of turbulence; (ii) stream-shear sources of 2D and slab turbulence only; and (iii) stream-shear sources of 2D and slab turbulence, and a PUI source of slab turbulence. For this, we used the nearly incompressible turbulence transport model equations of Zank et al. (2017a). We calculated the ratio of the 2D and slab magnetic field variances in the energy-containing and inertial ranges. As the Zank et al. (2017a) turbulence transport model equations are formulated in the energy-containing regime, the ratio of the 2D and slab magnetic field variances $\langle B_{2D}^2\rangle/\langle b_{slab}^2\rangle$ from the Zank et al. model provides the anisotropy in magnetic field fluctuations in the energy-containing range only. To compute the anisotropy in the inertial range, we exploited a fundamental assumption in the transport models (Zank et al. 1996a, 2012; Matthaeus et al. 1996), which is that the turbulence is fully developed with a self-similar inertial range that balances the rate of energy input to dissipation. This assumption corresponds to assuming either a Kolmogorov or an I-K inertial range spectrum. We then use a simple dimensional argument to estimate the anisotropy in the inertial range based on our computing the energy in the energy-containing range, i.e., Equation (15). Equation (15) describes the ratio of the variances of 2D and slab magnetic field fluctuations in the inertial range as a function of the 2D and slab fluctuating magnetic energy and corresponding correlation lengths in the energy-containing range. Using Equation (15), we calculated the evolution of the power anisotropy in magnetic field fluctuations in the inertial range throughout the heliosphere. We investigated the ratio of the 2D and slab magnetic field variances assuming inner boundary (1 au) 2D and slab energy ratios of 80:20, 70:30, 60:40, and 55:45, in the energy-containing range.

To determine whether there was an increasing trend in the evolution of the power anisotropy in magnetic field fluctuations observationally, we used *Ulysses* measurements to estimate $\langle B_{2D}^2\rangle/\langle b_{slab}^2\rangle$ from 1.5 to 4.5 au. Figure 5 shows the radial evolution of the power anisotropy observed in the outer heliosphere by the *Ulysses* spacecraft. In Figure 5, $P_\perp$ indicates the power of the magnetic field fluctuations in the direction perpendicular to the mean magnetic field, and $P_{||}$ the power in the direction parallel to the mean magnetic field. Each point refers to 30-day measurements acquired by *Ulysses* with a time cadence of 1 s, during the years 1996–1997 over a heliocentric distance from about 1.5 to 4.5 au. The power anisotropy here is the ratio between the perpendicular and parallel power spectra integrated over the frequency range 10^{-3}–10^{-2} Hz. To derive the perpendicular and parallel components of the magnetic field fluctuations, the spectral matrix of the magnetic field vector is first derived, by means of wavelet transforms, as a function of time and scale. The angle distribution of the magnetic field power spectrum in the interval $\theta_a < \theta_{VB} < \theta_b$ can then be constructed by averaging, scale by scale, the power values at those times for which the angle θ_{VB} between the local mean magnetic field and the wind direction ranges between θ_a and θ_b (Horbury et al. 2008). Finally, the parallel and perpendicular spectra are derived by averaging the inferred angular distribution of the spectral matrix in the ranges 0°–30° and 60°–90°, respectively. Although a more detailed observational study is warranted, the preliminary results illustrated in Figure 5 show that there is indeed an increasing trend in $\langle B_{2D}^2\rangle/\langle b_{slab}^2\rangle$ with increasing heliocentric distance, at least over part of the inertial range. Future studies will focus as a detailed comparison of the theory presented here and a suite of observations drawn from a variety of spacecraft.

Both our theoretical and observational studies show that the power anisotropy in magnetic field fluctuations in the energy-containing and inertial range increase slightly from ∼1.5 to ∼5-8 au. In addition, the theoretical results show that the anisotropies in the energy-containing and inertial range behave differently for the three turbulence source cases. We summarize our results for the three cases as follows:

(1) In the absence of in situ sources of turbulence, (i) the ratio $\langle B_{2D}^2\rangle/\langle b_{slab}^2\rangle$ in the energy-containing range exhibits a similar increasing trend with heliocentric distance for each energy ratio: (ii) the ratio in the inertial range also shows similar trends for each energy ratio, where the ratio increases until ∼20 au, and then decreases with increasing heliocentric distance; and (iii) the evolving anisotropy ratios in both the energy-containing and the inertial range are ordered by the inner boundary ratios and the curves track each other closely.

(2) When only a stream-shear source of turbulence is included in both the 2D and slab descriptions, we find (i) the ratios in the energy-containing and inertial ranges exhibit similar trends with heliocentric distance; (ii) the ratios in the energy-containing range increase initially, and then remain approximately constant and ordered

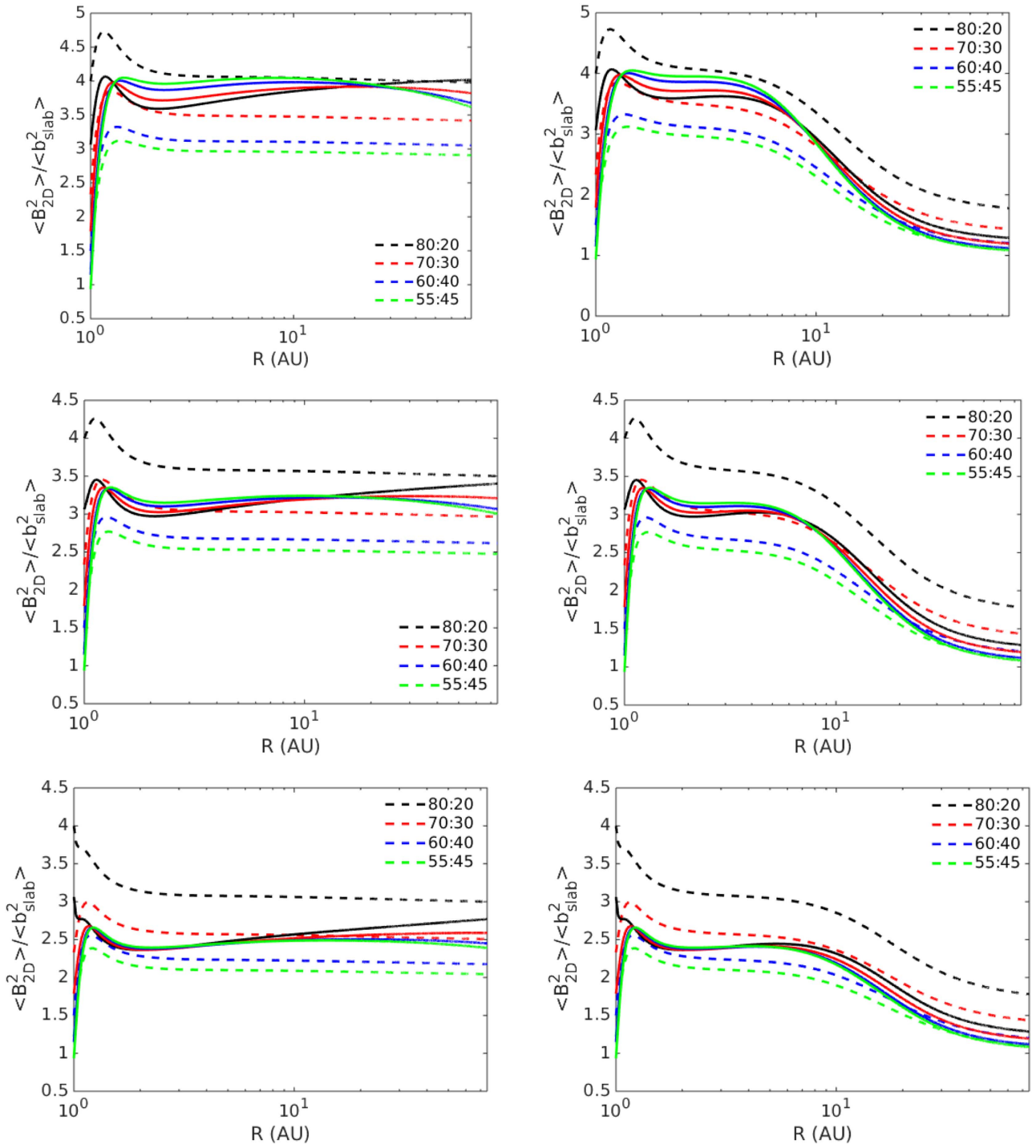

Figure 4. Evolution of the power anisotropy as a function of heliocentric distance for different assumptions about the turbulence source terms. Top panel plots use $C_{sh}^{\pm} = 0.9$, $C_{sh}^{ED} = -0.5$, $C^{*\pm}_{sh} = 0.45$, $C^{*ED}_{sh} = -0.25$, and $f_D = 0.25$; middle panel plots use $C_{sh}^{\pm} = 0.9$, $C_{sh}^{ED} = -0.5$, $C^{*\pm}_{sh} = 0.6$, $C^{*ED}_{sh} = -0.33$, and $f_D = 0.25$; and bottom panel plots use $C_{sh}^{\pm} = C^{*\pm}_{sh} = 0.9$, $C_{sh}^{ED} = C^{*ED}_{sh} = -0.5$, and $f_D = 0.25$. The left column corresponds to stream-shear sources of 2D and slab turbulence only. The right column corresponds to both a pickup ion source and stream-shear sources.

beyond ∼2 au according to the assumed inner boundary energy ratios; (iii) the ratio $\langle B_{2D}^2 \rangle / \langle b_{slab}^2 \rangle$ in the inertial range, black curve with initial energy ratio 80:20, increases monotonically with heliocentric distance from ∼2 to 75 au for each strength of stream-shear sources of 2D and slab turbulence; (iv) the ratios $\langle B_{2D}^2 \rangle / \langle b_{slab}^2 \rangle$ in the inertial range for the red, blue, and green curves, i.e., with initial energy ratios 70:30, 60:40, and 55:45, respectively, slightly increase from ∼2 to ∼10–20 au, and then slowly decrease with heliocentric distance for unequal stream-shear sources of 2D and slab turbulence; and (v) in the case of equal stream-shear sources of 2D and slab turbulence, the ratios for the solid black and red curves, i.e., with initial energy ratios 80:20 and 70:30, respectively, increase monotonically with distance from ∼2 to 75 au. However, the ratios for the solid blue and green curves, i.e., with initial energy ratios 60:40 and 55:45, respectively, increase monotonically from ∼2 to ∼10 au,

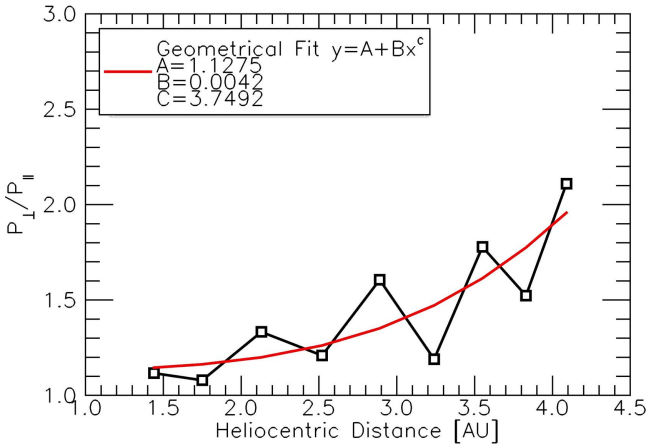

Figure 5. Evolution of the power anisotropy in magnetic field fluctuations measured by *Ulysses* as a function of heliocentric distance.

and then remain approximately constant until 75 au, and (vi) the ratios in the energy-containing and inertial ranges are small if stream-shear sources provide equal energy to 2D and slab turbulence, and are large if stream-shear provides unequal energy to 2D and slab turbulence.

(3) For the fully driven turbulence case that includes driving by both stream-shear and the creation of PUIs in the outer heliosphere, we find (i) the ratios in the energy-containing and inertial ranges exhibit similar trends throughout the heliosphere; (ii) the ratios in the energy-containing range increase initially, remain approximately constant, and then decrease beyond ∼6–10 au in similar fashion depending on the assumed inner boundary energy ratios; (iii) the ratios in the inertial range increase initially, decrease and then increase slightly from ∼2 to ∼5-8 au, which then decrease more rapidly from ∼8–30 au, and then more gradually until 75 au; and (iv) the ratios all converge to approximately the same ∼1 value in the outer heliosphere indicating that the fluctuations are almost isotropic.

Our theoretical analysis predictes interesting and testable properties about the anisotropy in magnetic field fluctuations throughout the heliosphere. *Ulysses* measurements provide the observed power anisotropy in between ∼1.5 to ∼4.5 au. We suggest that an anisotropy in magnetic fluctuations exists within ∼20 au, but the fluctuations in the outer heliosphere revert to an almost isotropic state. We can use a similar approach to study the anisotropy in solar wind velocity fluctuations and the Elsässer energies, a topic that will be addressed in subsequent work.

We acknowledge the partial support of NASA grants NNX08AJ33G, 478 Subaward 37102-2, NNX14AC08G, NNX14AJ53G, A99132BT, RR185-447/4944336, and NNX12AB30G. G.P.Z. is partly supported by the International Space Science Institute (ISSI), both through the award of the Johannes Geiss Fellowship 2017 and in the framework of International Team 504 entitled Current Sheets, Turbulence, Structures and Particle Acceleration in the Heliosphere. D.S. is partially supported by MEXT/JSPS KAKENHI grant numbers JP15K21709 and JP15H05813.

ORCID iDs

L. Adhikari https://orcid.org/0000-0003-1549-5256
G. P. Zank https://orcid.org/0000-0002-4642-6192
P. Hunana https://orcid.org/0000-0002-9860-9759
R. Bruno https://orcid.org/0000-0002-2152-0115
D. Shiota https://orcid.org/0000-0002-9032-8792

References

Adhikari, L., Zank, G. P., Hunana, P., et al. 2017a, Journal of Physics Conference Series, 900, 012001
Adhikari, L., Zank, G. P., Hunana, P., et al. 2017b, ApJ, 841, 85
Belcher, J. W., & Davis, L., Jr. 1971, JGR, 76, 3534
Bieber, J. W., Wanner, W., & Matthaeus, W. H. 1996, JGR, 101, 2511
Bruno, R., & Telloni, D. 2015, ApJL, 811, L17
D'Amicis, R., & Bruno, R. 2015, ApJ, 805, 84
Dasso, S., Matthaeus, W. H., Weygand, J. M., et al. 2008, Proc. ICRC (Mérida), 30, 625
Dasso, S., Milano, L. J., Matthaeus, W. H., & Smith, C. W. 2005, ApJL, 635, L181
Dong, Y., Verdini, A., & Grappin, R. 2014, ApJ, 793, 118
Ghosh, S., Matthaeus, W. H., Roberts, D. A., & Goldstein, M. L. 1998, JGR, 103, 23705
Goldreich, P., & Sridhar, S. 1995, ApJ, 438, 763
Grappin, R. 1986, PhFl, 29, 2433
Grappin, R., Velli, M., & Mangeney, A. 1993, PhRvL, 70, 2190
Horbury, T. S., Forman, M., & Oughton, S. 2008, PhRvL, 101, 175005
Hunana, P., & Zank, G. P. 2010, ApJ, 718, 148
Isenberg, P. A. 1986, JGR, 91, 9965
Isenberg, P. A. 2005, ApJ, 623, 502
Matthaeus, W. H., Dasso, S., Weygand, J. M., et al. 2005, PhRvL, 95, 231101
Matthaeus, W. H., Goldstein, M. L., & Roberts, D. A. 1990, JGR, 95, 20673
Matthaeus, W. H., Zank, G. P., & Oughton, S. 1996, JPlPh, 56, 659
Milano, L. J., Dasso, S., Matthaeus, W. H., & Smith, C. W. 2004, PhRvL, 93, 155005
Montgomery, D. 1982, PhyS, 1982, 83
Montgomery, D., & Turner, L. 1981, PhFl, 24, 825
Narita, Y., Glassmeier, K.-H., Sahraoui, F., & Goldstein, M. L. 2010a, PhRvL, 104, 171101
Narita, Y., Sahraoui, F., Goldstein, M. L., & Glassmeier, K.-H. 2010b, JGRA, 115, A04101
Osman, K. T., & Horbury, T. S. 2007, ApJL, 654, L103
Podesta, J. J. 2009, ApJ, 698, 986
Robinson, D. C., & Rusbridge, M. G. 1971, PhFl, 14, 2499
Ruiz, M. E., Dasso, S., Matthaeus, W. H., Marsch, E., & Weygand, J. M. 2011, JGRA, 116, A10102
Shalchi, A., Bieber, J. W., Matthaeus, W. H., & Schlickeiser, R. 2006, ApJ, 642, 230
Shebalin, J. V., Matthaeus, W. H., & Montgomery, D. 1983, JPlPh, 29, 525
Smith, C. W. 2003, in AIP Conf. Ser. 679, Solar Wind Ten, ed. M. Velli et al. (Melville, NY: AIP), 413
Velli, M. 2003, PPCF, 45, A205
Verdini, A., & Grappin, R. 2015, ApJL, 808, L34
Verdini, A., & Grappin, R. 2016, ApJ, 831, 179
Weygand, J. M., Matthaeus, W. H., Dasso, S., et al. 2009, JGRA, 114, A07213
Wicks, R. T., Horbury, T. S., Chen, C. H. K., & Schekochihin, A. A. 2010, MNRAS, 407, L31
Zank, G. P. 1999, SSRv, 89, 413
Zank, G. P. 2014, in Transport Processes in Space Physics and Astrophysics, ed. G. P. Zank (Berlin: Springer)
Zank, G. P., Adhikari, L., Hunana, P., et al. 2017a, ApJ, 835, 147
Zank, G. P., Adhikari, L., Hunana, P., et al. 2017b, Journal of Physics Conference Series, 900, 012023
Zank, G. P., Dosch, A., Hunana, P., et al. 2012, ApJ, 745, 35
Zank, G. P., Hunana, P., Mostafavi, P., & Goldstein, M. L. 2014, ApJ, 797, 87
Zank, G. P., & Matthaeus, W. H. 1991, PhFl, 3, 69
Zank, G. P., & Matthaeus, W. H. 1992, JGR, 97, 17189
Zank, G. P., Matthaeus, W. H., Bieber, J. W., & Moraal, H. 1998, JGR, 103, 2085
Zank, G. P., Matthaeus, W. H., & Smith, C. W. 1996a, JGR, 101, 17093
Zank, G. P., Pauls, H. L., Cairns, I. H., & Webb, G. M. 1996b, JGR, 101, 457
Zweben, S. J., Menyuk, C. R., & Taylor, R. J. 1979, PhRvL, 42, 1270